Earth and Space Science

RESEARCH ARTICLE
10.1029/2023EA003323

Retrieval of Rotational Temperatures From the Arecibo Observatory Ebert-Fastie Spectrometer and Their Inter-Comparison With Co-Located K-Lidar and SABER Measurements

Sukanta Sau[1], Pedrina Terra[2], Christiano G. M. Brum[2], Fabio A. Vargas[3], Jens Lautenbach[4], and S. Gurubaran[5]

[1]Equatorial Geophysical Research Laboratory, Indian Institute of Geomagnetism, Tirunelveli, India, [2]Florida Space Institute, University of Central Florida, Orlando, FL, USA, [3]University of Illinois at Urbana-Champaign, Urbana, IL, USA, [4]Inter-American University of Puerto Rico, Barranquitas, PR, USA, [5]Indian Institute of Geomagnetism, Navi Mumbai, India

Key Points:

- Good inter-comparison is obtained between Arecibo Observatory spectrometer and Lidar temperatures, and results are similar to previous studies
- The temperature comparison improves when time-varying weighting functions are used instead of a single weighting function
- Rotational temperature estimation from the spectrometer data depends strongly on the choice of Einstein coefficients for the P1 line transitions

Correspondence to:
S. Sau,
sukanta.sau@gmail.com

Citation:
Sau, S., Terra, P., Brum, C. G. M., Vargas, F. A., Lautenbach, J., & Gurubaran, S. (2024). Retrieval of rotational temperatures from the Arecibo Observatory Ebert-Fastie spectrometer and their inter-comparison with co-located K-Lidar and SABER measurements. *Earth and Space Science*, *11*, e2023EA003323. https://doi.org/10.1029/2023EA003323

Received 28 SEP 2023
Accepted 27 JAN 2024

Author Contributions:
Conceptualization: Sukanta Sau
Data curation: Sukanta Sau, Jens Lautenbach
Formal analysis: Sukanta Sau, Christiano G. M. Brum
Funding acquisition: Pedrina Terra
Investigation: Sukanta Sau
Methodology: Sukanta Sau, Christiano G. M. Brum, Fabio A. Vargas
Supervision: Pedrina Terra
Writing – original draft: Sukanta Sau
Writing – review & editing: Sukanta Sau, Pedrina Terra, Christiano G. M. Brum, Fabio A. Vargas, Jens Lautenbach, S. Gurubaran

Abstract Rotational temperatures in the Mesosphere-Lower Thermosphere region are estimated by utilizing the OH(6,2) Meinel band nightglow data obtained with an Ebert-Fastie spectrometer (EFS) operated at Arecibo Observatory (AO), Puerto Rico (18.35°N, 66.75°W) during February-April 2005. To validate the estimated rotational temperatures, a comparison with temperatures obtained from a co-located Potassium Temperature Lidar (K-Lidar) and overhead passes of the Sounding of the Atmosphere by Broadband Emission Radiometry (SABER) instrument onboard NASA's Thermosphere Ionosphere Mesosphere Energetics and Dynamics (TIMED) satellite is performed. Two types of weighting functions are applied to the K-Lidar temperature profiles to compare them with EFS temperatures. The first type has a fixed peak altitude and a fixed full width at half maximum (FWHM) for the whole night. In the second type, the peak altitude and FWHM vary with the local time. SABER measurements are utilized to estimate the OH(6,2) band peak altitudes and FWHMs as a function of local time and considerable temporal variations are observed in both the parameters. The average temperature differences between the EFS and K-Lidar obtained with both types of weighting functions are comparable with previously published results from different latitude-longitude sectors. We found that the temperature comparison improves when the time-varying weighting functions are considered. Comparison between EFS, K-Lidar, and SABER temperatures reveal that on average, SABER temperatures are lower than the other two instruments and K-Lidar temperatures compare better with SABER in comparison to EFS. Such a detailed study using the AO EFS data has not been carried out previously.

Plain Language Summary In the Earth's atmosphere, a strong band of near-infrared (NIR) emissions exists at ~90 km altitude due to the vibrational-rotational excitation of the Hydroxyl (OH) molecules. The intensity of these OH emissions depends on the temperatures of their rotational states. Under the assumption of thermodynamic equilibrium, the rotational temperatures should represent the background atmospheric temperatures. A scanning spectrometer of the Ebert-Fastie configuration (EFS) was operated on the nights of February-April 2005 at Arecibo Observatory (AO), Puerto Rico (18.35°N, 66.75°W) to record the intensity of the OH(6,2) band which is used to estimate rotational temperatures in this work. During the same period, a co-located Potassium temperature Lidar (K-Lidar) utilized resonance scattering from the atmospheric K-atoms to measure temperatures in the 80–100 km altitude range. By nature, the EFS-derived temperatures are an altitude-integrated quantity while the K-Lidar provides altitude-resolved temperatures. First, we followed a commonly used methodology to compare the EFS and K-Lidar temperatures by using the SABER data onboard NASA Thermosphere Ionosphere Mesosphere Energetics and Dynamics satellite. We found good agreement between our results and previously published studies. Then, we propose a modified methodology with the help of SABER data to show that it provides a better comparison between the EFS and K-Lidar temperatures.

1. Introduction

The mesosphere and lower thermosphere (MLT) region (approximately from 80 to 120 km altitude) is a unique part of the terrestrial atmosphere where both the neutral dynamics and plasma electrodynamics play crucial roles in governing the overall motion. This region is affected by dynamical processes from the lower altitudes, such as

atmospheric gravity waves, tides, planetary waves, etc., and external forcing from the higher altitudes, such as solar activity and geomagnetic storms. The MLT region plays a crucial role in the atmospheric vertical coupling processes, and it is essential to understand and quantify the variabilities of this region at different temporal and spatial scales.

It has been challenging to investigate the MLT temperatures since this region is too high for balloon sounding and too low for sustainable in-situ measurements by satellites (Bittner et al., 2002 and references therein). Limited in-situ measurements obtained with sounding rockets and falling spheres provide valuable MLT temperature information (Lübken, 1999; Nordberg et al., 1965). Space-based remote sensing instruments onboard low earth-orbiting satellites and ground-based remote sensing instruments, such as the meteor radar, incoherent scatter radar, and lidars, have helped to accumulate important MLT temperature databases in the past few decades (e.g., Fricke & von Zahn, 1985; Hocking, 1999; Höffner & Lautenbach, 2009; Russell et al., 1994; Tepley & Mathews, 1978). The discovery of the OH band emissions in the nightglow spectrum by Meinel (1950), provided another tool to monitor MLT temperatures remotely. Since then, ground-based optical instruments, such as the Ebert-Fastie spectrometer (EFS), have been employed to observe the intensity of these vibrational-rotational OH emission lines and estimate the temperatures in this region (e.g., Bittner et al., 2002; Sigernes et al., 2003).

EFS is capable of recording airglow emissions coming from different altitudes in the MLT region (e.g., O_2(0,1) atmospheric band and OH Meinel bands) in a single scan, and in turn, allows temperature estimation from these altitudes. The temperatures obtained from EFS are naturally weighted by the volume emission rate (VER) profile of the corresponding emission. Therefore, knowledge of the shape and peak altitude of these VER profiles is essential to understand these temperatures in a better way. Also, information about these two parameters of the VER is crucial for the inter-comparison between instruments that provide altitude-integrated measurements (such as EFS) and altitude-resolved measurements (such as Lidar, Meteor radar, and satellite).

To date, most of the observations with EFS have been carried out from either the high latitudes or the mid-latitudes stations (Bittner et al., 2002; Myrabø et al., 1984; Sigernes et al., 2003; Sivjee et al., 1972). Some of these stations have been operating the EFS continuously for several decades and have acquired valuable long-term MLT temperature data sets. To our knowledge, the EFS at the AO was the only one that continuously monitored MLT temperatures in the low-latitude regions. This EFS was brought to the AO from the Kitt Peak National Observatory, Arizona, USA, in the 1970s, and since then, it has been utilized to measure different airglow emissions (Burnside et al., 1977; Burnside et al., 1980; Meriwether Jr. et al., 1978; Meriwether Jr. & Walker, 1977; Tepley et al., 1981).

During its ∼40 years of operation, the AO EFS has been utilized to mostly observe the O_2 (0,1) atmospheric band and OH(6,2) and OH(8,3) Meinel band emission lines of the nightglow spectrum. This rich database offers the opportunity to pursue several interesting research topics related to the low-latitude MLT dynamics, such as, how the phenomena of sudden stratospheric warming and quasi-biennial oscillation modulate it, how the MLT temperatures respond to the geomagnetic disturbances and varying solar activity levels, variabilities of the nighttime MLT region due to tides and waves of different scales, etc. Despite the extensive database, only a few studies had been conducted in the past based on a single night or a few nights of these MLT region emissions data (Hecht et al., 1993; Kane et al., 1993; Meriwether, 1979; Walterscheid et al., 2000; Zhou et al., 1997).

This work is the first step of a new initiative that plans to investigate long-term trends in the MLT region with the help of the vast AO EFS MLT database and study their relationship with other geophysical parameters. Here, we present a methodology to estimate the rotational temperatures in the MLT region by using the intensity of the P1 lines of the OH(6,2) Meinel band measured by the AO EFS. A comparison with the co-located K-Lidar data and sounding of the atmosphere by broadband emission radiometry (SABER) measurements has been conducted to validate our results. In addition, we have studied how different factors influence the temperature comparison between EFS and K-Lidar, such as Einstein coefficients for line transition, and properties of the weighting function. The AO EFS data used in this work have not been explored before.

2. Instruments

A detailed description and working principle of the AO EFS can be found in Meriwether Jr. and Walker (1977) and Meriwether (1979). The AO EFS consists of a concave mirror with a 1 m focal length. The EFS is fitted with a mirror system at the top, allowing it to look at different elevations and azimuth angles. During the period of our

Table 1
List of the Dates When EFS and K-Lidar Data Are Available Simultaneously During the Study Period

Serial no.	Dates when AO EFS and K-lidar data are available simultaneously	Availability of SABER passes over AO during these dates
1	07 February 2005	No
2	08 February 2005	No
3	09 February 2005	No
4	10 February 2005	Yes
5	11 February 2005	No
6	05 March 2005	No
7	10 March 2005	Yes
8	12 March 2005	No
9	13 March 2005	Yes
10	14 March 2005	No
11	17 March 2005	Yes
12	08 April 2005	No
13	09 April 2005	No
14	10 April 2005	Yes
15	14 April 2005	No

Note. The availability of SABER data on these dates is also indicated here.

study, the instrument was pointed toward the zenith, and it was operated in the first order with a slit width of 0.6 mm × 8 mm. These settings provide a spectral resolution of ∼4.5 Å and a field of view (FoV) of ∼1° × 8° (Kerr et al., 2001). This spectral resolution is sufficient to resolve the P1 rotational lines of the OH(6,2) Meinel band. To prevent higher-order emission lines from appearing in the spectrum, a blocking filter was used which allows wavelength in the range of 6,900–29,000 Å to pass through with an average transmissivity of ∼86%. A Hamamatsu R943-02 series photomultiplier tube (PMT) was utilized as the photon detector. The photocathode of the PMT is made of GaAs and it has very good sensitivity in the range of ∼3,000–8,300 Å. The integration time per spectral point varies between 1.7 and 3.3 s on different nights during the study period, resulting in variable data cadence between 6.8 min and 13.2 min. Dark count data for a particular night is obtained with a similar integration time per spectral point as the airglow data. An Argon (Ar) lamp was used to calibrate the AO EFS wavelength coverage. The sensitivity of the EFS was calibrated with the help of a Tungsten lamp operated at 6.25 A at 24 V.

The K-Lidar used in this work has been continuously operated at AO since early 2000 (Friedman et al., 2003). It sends out pulses of an Alexandrite Ring Laser that is injection seeded by a continuous wave (CW) laser and collects the backscattered laser light from the atmosphere with an 80 cm mirror, as described in detail by Friedman (2003). The well-established three-frequency technique measures mesospheric temperature from the Potassium spectra by switching between three laser frequencies (Friedman, 2003; She & Yu, 1994). The CW seed laser is locked to a Doppler-free feature at the K-D1 line near the peak of the K fluorescence to establish the frequency reference. An acousto-optic modulator setup generates and switches to the two wing frequencies. The signal is integrated for 1,000, and 500 laser pulses at the reference frequency and the two wing frequencies, respectively, with a range resolution of 150 m. In routine operations, the raw data are processed to extract temperature profiles with a resolution of 30 min and 450 m. The resulting temperature errors are about 2–3 K and <50 K at the peak and edge of the K layer, respectively (Friedman & Chu, 2007). However, temperatures utilized in this study are processed with a temporal resolution of 15 min to match the EFS data resolution better, resulting in an increased error by ∼1.5–2 times at the peak and by ∼2–3 times at the edge of the K layer in comparison to the 30 min resolution data. Data gaps in the temperature profiles due to weak signals (e.g., edge of the K-layer, clouds, or "bad" laser pulses) are rare. Friedman and Chu (2007) describe the instrument improvements implemented in 2003 to extract reliable and precise raw data by discrimination against spectrally "bad" pulses from the Alexandrite Ring laser or secondary frequencies bleeding of the single-frequency CW seed laser.

In this study, data from the SABER instrument onboard NASA's Thermosphere Ionosphere Mesosphere Energetics and Dynamics (TIMED) satellite has also been used. A detailed description of the SABER instruments and the parameters they measure is documented by Russell et al. (1994) and Esplin et al. (2023). We have utilized the SABER 2.07 version of the channel A and channel B VER data which are estimated at 2.0 and 1.6 μm wavelength, respectively. The SABER channel A data is constituted of OH(9,7) and OH(8,6) Meinel band line emissions, while channel B contains the OH(5,3) and OH(4,2) Meinel band emissions. We have also used MLT region kinetic temperatures retrieved by SABER from the observations of CO_2 limb emission at 15 μm wavelength. It has been shown that the uncertainties in the SABER kinetic temperatures are within the range of ±1.5 K below 95 km altitude (García-Comas et al., 2008). The altitude resolution of the SABER 2.0 and 1.6 μm VER data as well as kinetic temperatures is ∼0.4 km between 80 and 95 km altitude.

3. Methodology and Data Analysis

EFS and K-Lidar data during the period of February–April 2005 are considered in this work. This period is characterized by good weather and clear sky nights over AO, resulting in more simultaneous EFS and K-lidar observation than in other months. A total of 15 nights of simultaneous EFS and K-Lidar data are available during the study period, which results in ∼90 hr of concurrent good-quality data. The dates corresponding to these 15 nights and the availability of SABER passes over AO on these nights are mentioned in Table 1. In this study as well as in Table 1, any date (e.g., 07 February 2005) generally denotes the period between the evening of that date (i.e., 18:00 Atlantic Standard Time (AST) on 07 February 2005) and the morning of the next date (i.e., 06:00 AST on 08 February 2005 or 30:00 AST on 07 February 2005), unless specified otherwise. Atlantic Standard Time = Universal Time Coordinate −4 hr.

3.1. Rotational Temperature Estimation From EFS Data

Rotational temperatures in the MLT region are estimated by processing the raw airglow spectra recorded by the AO EFS. During this study period, each EFS spectrum consists of 240 spectral points. Each spectral point is hereafter referred to as a channel (*ch.*). To determine which *ch.* in the raw spectrum corresponds to which airglow wavelength, we have used the wavelength calibration data. If wavelength calibration data for a particular night is unavailable, then the calibration data available on the nearest previous night is considered. An example of wavelength calibration data is shown in Figure 1a. The channel number (*ch.no.*) and corresponding wavelengths of the four Argon (Ar) lines present in Figure 1a are noted in the first and second columns of Table 2, respectively. At times, the intensity profile for a particular Ar line peak appears to be slightly asymmetric with respect to the peak (e.g., the second Ar line peak in Figure 1a). Thus, to better estimate the Ar line peak locations, we have applied intensity weighted *ch.no.* method following Equation 1.

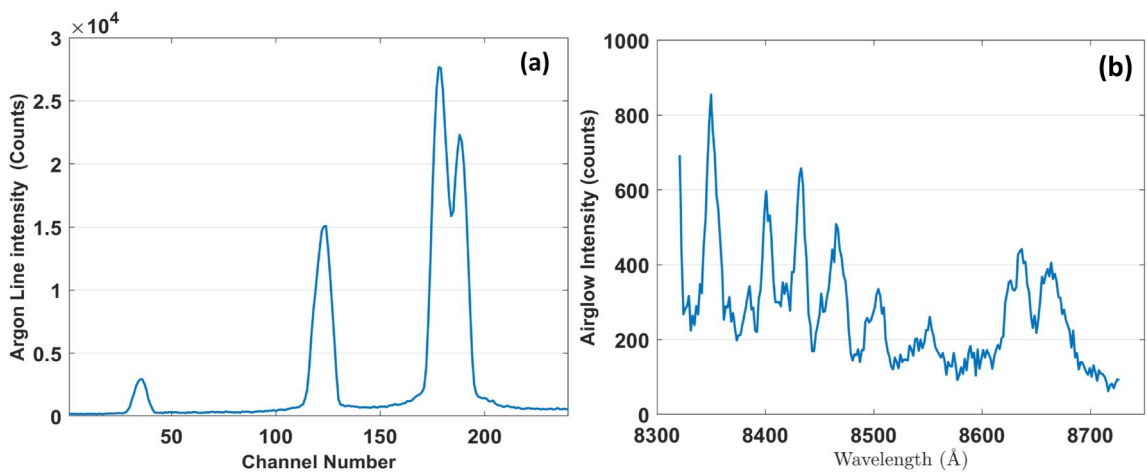

Figure 1. (a) Example of wavelength calibration of the AO EFS performed by using an Argon lamp between 18:56 AST and 18:58 AST on 10 February 2005. (b) A wavelength-calibrated raw AO EFS spectrum recorded between 20:44 AST and 20:57 AST on 11 February 2005.

Table 2
Details of the Wavelength Calibration Performed With the Help of an Argon Lamp on 10 February 2005

Peak *ch.no.* (raw data)	Standard Ar line wavelength (Å)	Intensity weighted *ch.no.* (Ch_p)	Fitted wavelength to Ch_p (Å)	Difference between columns 2 and 4 (Å)
36	8667.944	35.098	8668.504	−0.560
124	8521.442	122.596	8520.2	1.242
178	8424.647	179.275	8424.134	0.513
188	8408.210	187.965	8409.404	−1.194

$$Ch_p = \frac{\sum_{i=1}^{n} Ch.\ no.\ (i) \times I(i)}{\sum_{i=1}^{n} I(i)} \quad (1)$$

where Ch_p represents the estimated peak *ch.no.* of an Ar line, I and n represent intensity counts and the number of data points within the full width at half maximum (FWHM) of that peak. A linear fit between the Ar line wavelengths and Ch_p (column 3, Table 2) reveals that on 10 February 2005, *ch.* 1 and *ch.* 240 of the raw data correspond to 8726.3 Å and 8321.21 Å, respectively. This results in a data resolution of 1.688 Å/*ch.* The differences between observed and fitted wavelengths are within ±1.3 Å for all the nights during our study period. A wavelength-calibrated AO EFS raw spectrum is shown in Figure 1b. The five prominent peaks between 8,390 Å and 8,570 Å in Figure 1b belong to the P1 lines of the OH(6,2) Meinel band.

After that, dark counts are deducted from the raw spectrum counts shown in Figure 1b. Usually, dark counts are measured on each observation night. If dark counts are unavailable for a particular night, then dark counts from the nearest previous night are considered. Typical root mean square (RMS) dark count on a night lies in the range of 1–3 counts per second. The optical throughput of the EFS and the sensitivity of the PMT varies with wavelength. Therefore, sensitivity calibration of the EFS spectrum is required to rectify the effects of these two factors in the output counts. In our case, sensitivity calibration was performed by a low brightness Tungsten lamp (150 W, 6.25 A) housed in a box. Configuration of the EFS is kept the same during sensitivity calibration and recording of airglow spectra. The inside surfaces of the low-brightness source (LBS) box were painted black to minimize internal reflections. The absolute brightness of the LBS box in the wavelength range of 4,000–7,500 Å was obtained by calibrating it against the AO Carbon-14 source. To derive the absolute brightness of the LBS box in the wavelength range of the AO EFS spectrum, we have fitted the equation developed by Saunder at the National Institute of Standards (Equation 2) to the absolute brightness values between 4,000 Å and 7,500 Å following Sigernes et al. (2007). The results of this exercise are shown in Figure 2a.

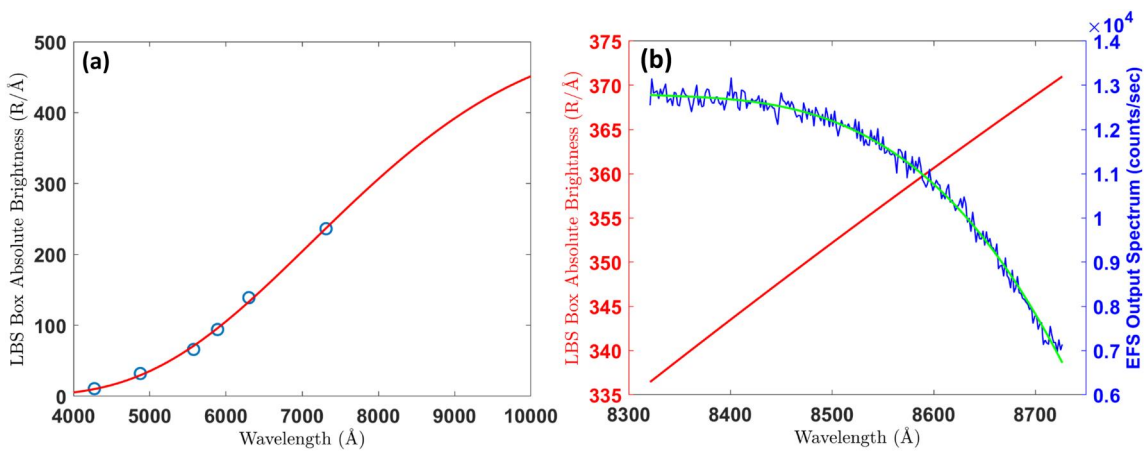

Figure 2. (a) Absolute Brightness of the low-brightness source (LBS) box obtained by calibrating it against a Carbon-14 source (open blue circles) and by fitting Equation 2 to these experimentally obtained brightness values (red line). (b) An EFS output spectrum obtained by using the LBS Box as the source on 10 February 2005 (blue line) and third-order polynomial fit to it (green line). The red line shows the absolute brightness of the LBS box in the same wavelength range.

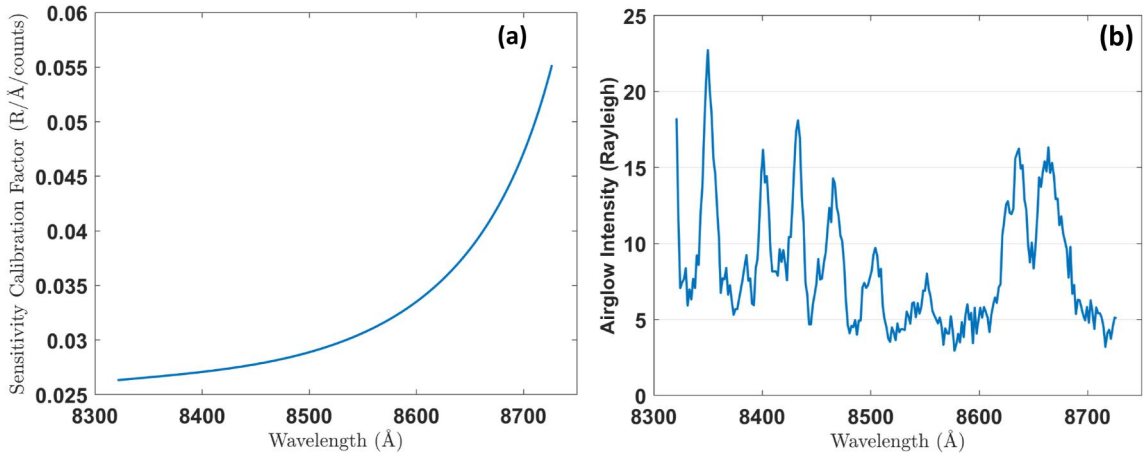

Figure 3. (a) Variation of sensitivity calibration factors with wavelength. (b) Sensitivity calibrated EFS spectrum obtained from the raw EFS spectrum shown in Figure 1(b).

$$B_\lambda \approx \lambda^{-5} \exp\left(a - \frac{b}{\lambda}\right) \times \frac{4\pi}{10^6} \tag{2}$$

Where B_λ represents lamp brightness in Rayleigh per Å and λ denotes wavelength in Å. In our case, the value of constants a and b turns out to be 69.46 and 60,110, respectively. An example of an EFS output spectrum obtained by using the LBS box as a source and the corresponding B_λ values are shown in Figure 2b. A third-order polynomial is fitted to the actual EFS output spectrum counts to estimate the mean output counts. It can be seen from Figure 2b that the EFS output counts decrease sharply after ~8,500 Å due to the poor sensitivity of the R943-02 series PMT at this wavelength range.

The ratio of the LBS box absolute brightness and the mean EFS output counts provides the sensitivity calibration factors that are applied to the DC-removed EFS spectrum. The result of this analysis is depicted in Figure 3. The final step before rotational temperature estimation is to remove the background intensity. We have considered the average intensity of seven channels (~12 Å) about 8,720 Å as the background intensity since they have the lowest values compared to all other channels in the data, and there is no prominent rotational line peak in those channels. In addition, the EFS data files contaminated by clouds or haze conditions have not been considered for temperature estimation. Data from a co-located all-sky imager operated by Boston University is utilized to detect sky conditions over AO.

Rotational temperature estimation by using the AO EFS data is based on the assumption that the P1 lines of the OH(6,2) Meinel band follow the Boltzmann distribution. Considering the collision frequency and lifetime of the excited Hydroxyl molecules (OH*), only those P1 lines with the rotational quantum number (K) < 6 follow the Boltzmann distribution for the $v' = 6$ level (Holmen et al., 2014; Pendleton Jr. et al., 1993). Therefore, we utilize only the P1 ($K = 2$ to $K = 5$) line intensities in the rotational temperature estimation. In addition, it is assumed that the vibrational-rotational states of OH* are in local thermodynamic equilibrium, which allows the rotational temperature to represent the neutral atmospheric temperature.

Assuming that the P1 rotational lines of the OH(6,2) band follow the Boltzmann distribution, the intensity (I) of each of these lines can be expressed as

$$I_{v',J' \to v'',J''} = N_{v'} A_{v',J' \to v'',J''} \left[\frac{2\left(2J'+1\right) hcB_v}{k_B T}\right] \times \exp\left(-\frac{F\left(J'\right) hc}{k_B T}\right) \tag{3}$$

Here, J, h, c, k_B, and T represent the rotational quantum number, Planck's constant, speed of light in space, Boltzmann constant, and rotational temperature, respectively. $N_{v'}$ represents the total concentration of OH*

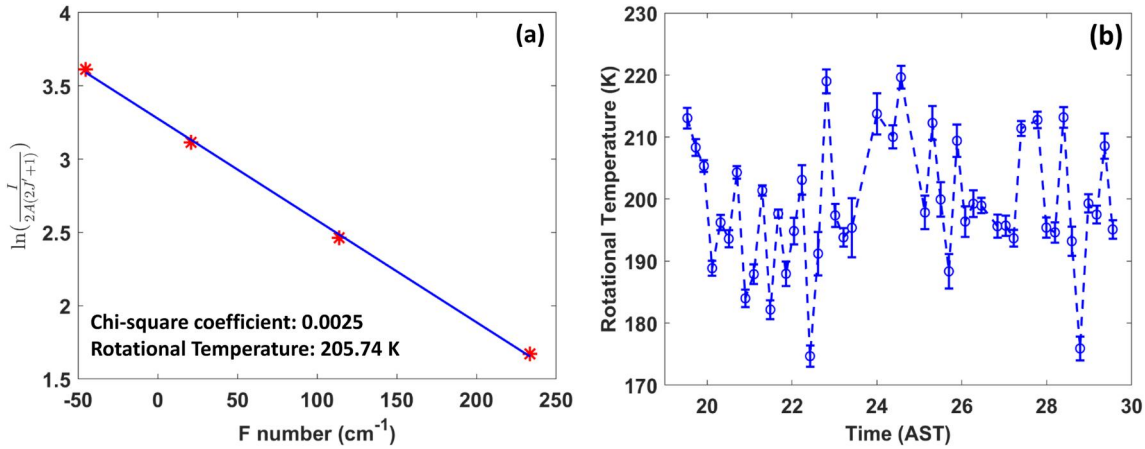

Figure 4. (a) An example of a Boltzmann plot corresponding to the P1 ($K = 2$ to $K = 5$) rotational lines shown in Figure 3(b). The blue color line denotes the linear fit. (b) Variation of rotational temperatures with time on the night of 10 March 2005. The blue circles depict the magnitude of rotational temperatures, and the blue vertical lines represent temperature measurement uncertainties.

molecules at the vibrational level v'. The term $A_{v',J'\rightarrow v'',J''}$ (henceforth denoted by A) represents the Einstein coefficient for a particular line transition. The rotational constant B_v and the rotational term $F(J')$ are obtained following Krassovsky et al. (1962).

By taking the logarithm of both sides of Equation 2 and rearranging the terms, the following expression can be obtained,

$$\ln\left(\frac{I}{2A\left(2J'+1\right)}\right) = \ln\left(\frac{N_{v'}hcB_v}{k_BT}\right) - \frac{F\left(J'\right)hc}{k_BT} \tag{4}$$

The plot of $\ln\left(\frac{I}{2A(2J'+1)}\right)$ against the rotational term $F(J')$ is called the Boltzmann plot. An example of a Boltzmann plot is shown in Figure 4a. The rotational temperature is estimated from the slope of the linear fit (i.e., $-\frac{hc}{k_BT}$). A chi-square test is performed to evaluate the goodness of the fitting in the Boltzmann plots. To ensure that the assumption of Boltzmann distribution is valid for our calculations, only those rotational temperatures are considered in this study where the chi-square coefficient is less than 0.05.

The uncertainties in the rotational temperature (σ_T) are calculated following the noted error propagation method (Vargas, 2019). The RMS value of σ_T varies between 1.5 and 5.5 K during our study period. An example of the variation of rotational temperatures derived from the AO EFS during a night is shown in Figure 4b, along with the corresponding measurement uncertainties.

3.2. Weighted Temperature Calculation From K-Lidar Temperature Profiles

The AO K-Lidar provides temperatures between 80 and 100 km with an altitude resolution of 0.45 km. The K-Lidar temperature profiles must be weighted by the OH(6,2) band VER to compare them with the EFS temperatures (Vargas et al., 2021). Any direct measurement of the OH(6,2) band VER is unavailable. Therefore, the SABER 1.6 μm VER profiles are utilized as the weighting function since their peak emission altitudes are expected to be close to that of the OH(6,2) band (von Savigny et al., 2012). SABER passes within ±2.5° latitude and longitude range of the AO and between 18:00 AST and 30:00 AST are only considered here. Out of the 15 nights when EFS and K-Lidar data are available concurrently, only on five nights do the SABER passes satisfy these two selection criteria (Table 1).

Two different methods are adapted to weight the K-Lidar temperature profiles. In both methods, K-Lidar temperature profiles are weighted by the observed SABER 1.6 μm VER profiles on those five nights when SABER data are available simultaneously with EFS and K-Lidar data. All the available SABER 1.6 μm VER profiles are

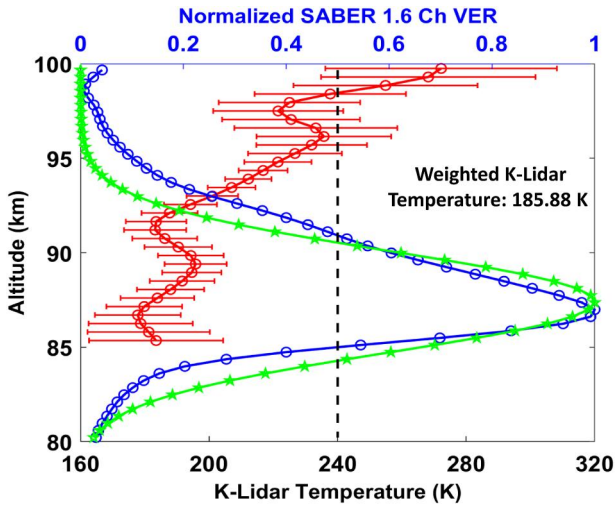

Figure 5. An example of a K-Lidar temperature profile obtained on 10 February 2005 at 29:45 AST from AO. The red open circles and red horizontal lines represent the magnitude and uncertainties of the Lidar temperatures, respectively. The solid blue line depicts a normalized SABER 1.6 μm *ch.* VER data recorded on 10 February 2005 at 30:00 AST over AO while the green line represents a Gaussian fit to it. The black dotted line marks $x = 0.5$ on the upper x-axis.

considered on these five nights irrespective of whether they have single peak or double peaks. Since the altitude resolution of the K-Lidar and SABER 1.6 μm VER data is different, the SABER 1.6 μm VER data is interpolated to the altitudes of the K-Lidar temperature profiles. In the first method, a Gaussian function having fixed peak altitude and FWHM is used to weight the K-Lidar temperature profiles on the remaining 10 nights (Table 1). Previous studies indicate that a Gaussian is a good approximation of the OH VER profile (e.g., Dunker, 2018 and references therein). The peak altitude and FWHM of the Gaussian function are the average values of the corresponding parameters obtained from the five nights of simultaneously available SABER 1.6 μm VER profiles: 87.05 ± 1.46 km and 6.46 ± 0.9 km, respectively. For any SABER 1.6 μm profile, the altitude having the maximum VER is considered as its peak altitude. The altitude difference between those two points which have VER ≈ 0.5*Maximum VER and are closest to the peak altitude, is considered as the FWHM of the SABER 1.6 μm profiles. In this study, we have followed the same method to estimate peak altitude and FWHM unless otherwise specified. We have not considered those SABER 1.6 μm VER profiles in this calculation that exhibit double peaks within the half maximum of the VER. This combination of observed SABER OH1.6 μm VER profiles as weighting functions on five nights and the Gaussian as the weighting function on the remaining 10 nights is termed "method-1." An example of a K-Lidar temperature profile and a SABER 1.6 μm VER profile recorded on the same night are shown in Figure 5.

It can be noticed from Figure 5 that the peak altitude of the Gaussian fit differs by ~0.45 km from the SABER OH1.6 μm VER and their FWHMs are comparable but their shapes are different. Therefore, to have a more realistic weighting function, we decided to construct an average VER profile. Eight single peak SABER OH1.6 μm VER profiles available concurrently with the EFS and K-Lidar data on the five nights (Table 1) are considered in this calculation. First, we decompose each of the OH1.6 μm VER profiles into two Gaussian components (Figure 6a). One of the two Gaussian components always has a higher peak altitude. The area, peak altitude, and FWHM of these two sets of Gaussians having higher and lower peak altitudes are then

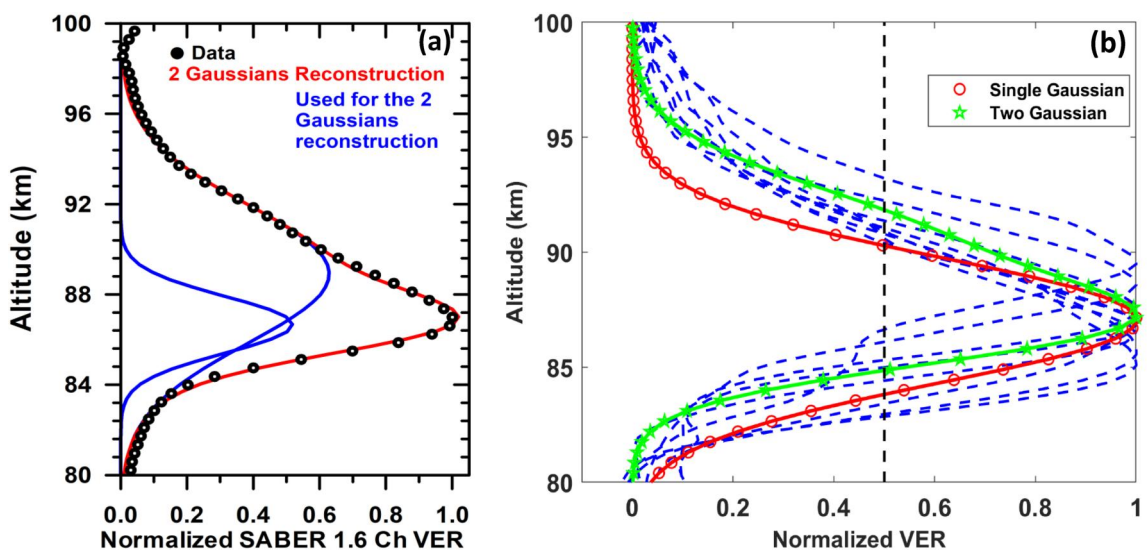

Figure 6. (a) The black circles represent the normalized SABER OH1.6 μm VER shown in Figure 5. The blue lines depict the two Gaussian components corresponding to the SABER OH1.6 μm VER. The sum of the two Gaussians is shown by a red line. (b) The blue dotted lines represent the eight SABER OH1.6 μm VERs concurrently available with the EFS and K-Lidar data. The average OH1.6 μm VER obtained from these eight VERs is shown by the solid green line. The solid red line represents the Gaussian used in method-1 (peak altitude: 87.05 km, FWHM: 6.46 km).

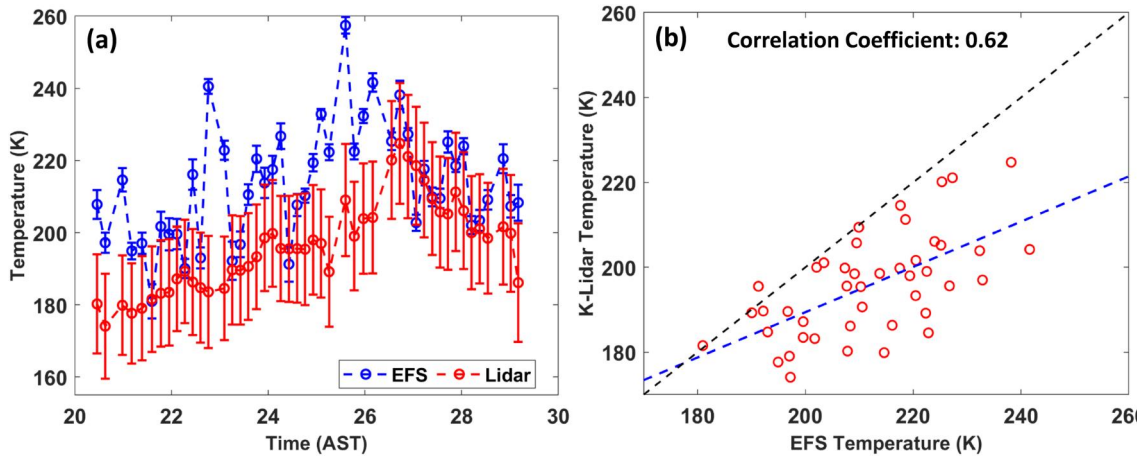

Figure 7. (a) Comparison of the EFS rotational temperatures (blue color) and weighted K-Lidar temperatures (red color) for 09 April 2005. Vertical lines of the corresponding color show the uncertainties in these two sets of temperatures. (b) Scatter plot of weighted K-Lidar temperatures as a function of EFS temperatures for the same night as in panel (a). The blue dotted line is the linear fit between these two temperatures while the black dotted line represents a linear fit having slope = 1.

averaged separately. These average parameters are used to construct two new Gaussians whose addition provides us with the average OH1.6 μm VER. All eight SABER OH1.6 μm VER profiles and their average profile are shown in Figure 6b. The combination of the observed SABER OH1.6 μm VER profiles as weighting function on the five nights and the average SABER OH1.6 μm VER profile (Figure 6b) as the weighting function on each of the remaining 10 nights, will henceforth be called "method-2."

Reliable temperature retrieval from the K-Lidar below 82–83 km is frequently hindered due to very low K atom densities on the edge of the K-layer. To ensure symmetric weighting on both sides of the Gaussian peak altitude, the minimum weighting factor limit is set at 0.5. In addition, Lidar profiles where temperatures are unavailable at any altitudes having a weight factor of ≥0.8 are not considered in the calculation to make sure that there is no bias in the weighted K-Lidar temperatures due to data gaps.

4. Results and Discussion

4.1. Comparison Between EFS and K-Lidar Temperatures Using a Fixed Weighting Function

In this section, we discuss temperature differences between EFS and K-Lidar when a weighting function having a fixed peak altitude and fixed FWHM is applied to the K-Lidar profiles for the whole night. The time resolution of the EFS and K-Lidar data is not equal, and at times, there are data gaps in both of these data sets. Thus, to better compare these two data sets, we have linearly interpolated the weighted K-Lidar temperatures at the time points of the EFS temperatures.

4.1.1. Comparison Between EFS and K-Lidar Temperatures Using Method-1

Here the K-Lidar temperatures on the nights mentioned in Table 1 are weighted by applying method-1 to compare them with EFS temperatures. A comparison between the EFS temperatures and interpolated weighted K-Lidar temperatures for the night of 09 April 2005 is shown in Figure 7a. The uncertainties in the weighted K-Lidar temperatures are the weighted mean of the individual temperature uncertainty at each altitude. The same weighting function which is used to weight the K-Lidar temperatures is also used to weight the temperature uncertainties. It can be seen from Figure 7a that the temporal trends of both data sets show a very good match. Though their magnitudes exhibit a very good match at certain times, in general, the EFS temperatures are found to be greater than the weighted K-Lidar temperatures during most of the nights. The K-Lidar temperatures are plotted as a function of EFS temperatures in Figure 7b where we have only considered K-Lidar temperatures within two standard deviations of the mean temperature difference to remove outliers. It is evident from Figure 7b that there is a good correlation between these two data sets and a positive bias exists in the EFS temperatures in comparison to the K-Lidar temperatures.

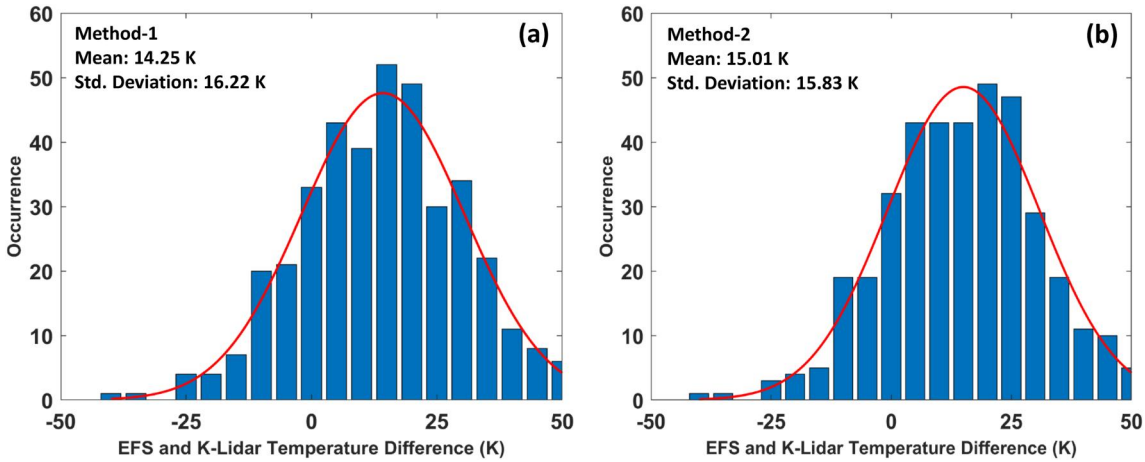

Figure 8. (a) Distribution of EFS and weighted K-Lidar temperature differences during February–April 2005 using method-1. The size of the individual bin is 5 K. The red line represents a Gaussian fit to the occurrence in the bins. The parameters of the Gaussian fit are mentioned in the upper left corner. (b) A plot similar to panel (a) of this Figure but using method-2.

In Figure 8a, differences between the EFS and weighted K-Lidar temperatures obtained by using method-1 for all 15 nights are plotted into bins of 5 K irrespective of their local time distribution. It is observed that there are 40.41%, 55.7%, and 69.43% points within the temperature difference range of ±10 K, ±15 K, and ±20 K, respectively. Considering the ∼1–6 K uncertainties in the EFS temperatures and much larger uncertainties (11–33 K) in the weighted K-Lidar temperatures, the results obtained here indicate that, in general, there is a good agreement between the EFS and K-Lidar temperatures. By fitting a Gaussian to the occurrences shown in Figure 8a, it is found that, on average, the EFS temperatures are warmer than the weighted K-Lidar temperatures by 14.25 K.

4.1.2. Comparison Between EFS and K-Lidar Temperatures Using Method-2

In this exercise, K-Lidar temperatures on the nights listed in Table 1 are weighted by using method-2. Temperature differences between the EFS and K-Lidar are plotted in Figure 8b by using the same procedure that is followed to prepare Figure 8a. It is observed that there are 40.52%, 53.0%, and 66.75% points within the temperature difference range of ±10 K, ±15 K, and ±20 K, respectively, which are very similar to the values obtained using method-1. However, the mean temperature difference obtained by using method-2 is larger by 0.75 K in comparison to method-1. It can be noted from Figure 6b that the peak altitude of the Gaussian weighting function used in method-1 and the average SABER 1.6 μm VER used in method-2 is the same. However, the FWHM of the weighting function in method-2 is ∼0.5 km larger in comparison to method-1. Also, in the case of method-2, equivalent weight factors are situated at higher altitudes on both sides of the peak in comparison to method-1 (Figure 6b). A combination of these factors is likely to cause a higher mean temperature difference between EFS and K-Lidar for method-2.

Table 3
Comparison Between Simultaneous EFS, Weighted K-Lidar, and Weighted SABER Temperatures

Date (yyyymmdd)	Average time of SABER pass (AST)	Average SABER OH1.6 μm temp. (K)	Average EFS temp. (K)	(EFS—SABER) temp (K)	Average K-lidar temp. (K)	(K-lidar—SABER) temp (K)
20050210	20.964	187.914 ± 3.217	198.573 ± 0	10.659	NaN	NaN
20050210	30.002	186.319 ± 0.266	NaN	NaN	202.126 ± 22.982	15.807
20050310	24.788	185.556 ± 1.291	218.17 ± 0	32.614	182.592 ± 7.023	−2.964
20050313	23.995	205.841 ± 0	218.817 ± 1.001	12.976	173.716 ± 11.699	−32.125
20050317	23.484	200.925 ± 0	202.405 ± 7.856	1.48	248.462 ± 0	47.537
20050410	22.078	194.545 ± 1.829	215.086 ± 1.318	20.541	200.5 ± 4.324	5.955

4.1.3. Comparison Between Simultaneous EFS, K-Lidar, and SABER Temperatures

We have also compared EFS temperatures with simultaneous weighted K-Lidar and weighted SABER temperatures. Weighted K-Lidar and SABER temperatures are obtained by multiplying normalized SABER OH1.6 μm VER with K-Lidar and SABER temperature profiles, respectively. All the criteria set for the weighting functions in the last paragraph of Section 3.2 also apply here. The results are summarized in Table 3. The average of EFS and weighted K-Lidar temperatures within ±15 min of the average time of SABER passes over AO are shown in columns four and six of Table 3, respectively. Zero standard deviation implies that only one data point is available within the ±15 min time range. It is apparent from Table 3 that EFS temperatures are always greater than the SABER temperatures, while the K-Lidar temperatures are both greater and smaller than the SABER temperatures. The average temperature differences of EFS and K-Lidar with SABER are 15.65 ± 11.67 K and 6.84 ± 28.95 K, respectively. It implies that, on average, the EFS temperatures are 8.81 K greater than the K-Lidar temperatures. However, it should be noted that these results are obtained by using only 10 passes of SABER. To arrive at a statistically significant result, analysis of a much more extensive database is required.

4.1.4. Comparison of Results With Previous Studies

We could find only two previous works where temperatures estimated by EFS and Lidar have been compared. Friedman et al. (2003) compared one night of temperature data obtained from the same set of instruments used in the present study. They did not quantify the temperature difference between these two instruments. Rather, they observed that the EFS temperatures compare well with the K-Lidar temperatures when K-Lidar temperatures at different altitudes are considered at different times. In other words, the EFS and K-Lidar temperatures compare poorly when Lidar temperature at a fixed altitude is considered for the whole night. Yu et al. (1991) compared temperatures estimated by an EFS onboard a scientific flight with temperatures obtained by a ground-based Na-Lidar. They noted temperature differences of ∼5–10 K during the closest approach of the flight to the Na-Lidar location.

In a few other studies, MLT temperatures retrieved by Lidar are compared with spectrometers that have different configurations than the EFS. Von Zahn et al. (1987) analyzed three nights of MLT temperatures obtained from a Czerny-Turner spectrometer and a co-located Na-Lidar. They found that the hourly averaged temperature differences were in the range of −10 to 5 K while the nightly mean temperatures were almost equal except for one night. She and Lowe (1998) have compared MLT temperatures estimated by a Fourier transform spectrometer and a Na-Lidar where the instruments were located at similar latitudes but 24° apart in longitudes. They reported an average difference of 9 K between nightly mean spectrometer temperatures and Na-Lidar temperatures at 87 km when both instruments were operating concurrently. Burns et al. (2003) conducted a comparative study of the temperatures derived by a Czerny-Turner spectrometer and a Na-Lidar where these two instruments are located at a distance of ∼1,500 km. They noticed that on one set of nights (∼56%) the average nightly mean temperature differences were close to zero while on the other set of nights (∼44%), the average differences turned out to be greater than 10 K. Dunker (2018) studied temperature difference between a co-located Czerny-Turner spectrometer and Na-Lidar. By employing a Gaussian function with fixed peak altitude and fixed shape to weight the Na-Lidar, they obtained nightly mean temperature differences in the range of −20 to 12 K.

We have not employed hourly average or nightly mean of the EFS and K-Lidar temperatures in our analysis like the previous comparison studies mentioned above. Therefore, the EFS and K-Lidar temperatures used in our analysis contain perturbations due to waves and tides of different spatial and temporal scales. Despite that, we find good agreement between the average temperature difference obtained in our study and the previous studies. However, the standard deviation is larger in our case in comparison to theirs.

4.1.5. Discussion on the Controlling Factors of the EFS and K-Lidar Temperature Difference

Several factors could contribute to the temperature differences observed in the present study. The peak altitude and FWHM of the weighting function applied on the K-Lidar temperature profiles play a crucial role in the intercomparison of EFS and K-Lidar temperatures since the maximum weighting is contributed by the altitudes surrounding the peak. Previous studies have indicated that OH Meinel bands' peak altitude and FWHM vary considerably over a longer period (Baker & Stair, 1988; Mulligan et al., 2009) as well as over a single night (Takahashi et al., 2005; Zhao et al., 2005). It is evident from Figure 6b that the peak altitude and FWHM of the SABER OH1.6 μm VER change significantly with local time, even when only a few profiles are considered.

Table 4
Comparison of EFS and K-Lidar Mean Temperature Difference During February–April 2005 by Using Different Einstein Coefficients

Method	Mies	LWR	TL	Loo	Hitran
Method-1	18.82 K ± 16.41 K	14.25 K ± 16.22 K	25.15 K ± 16.66 K	15.53 K ± 16.28 K	19.58 K ± 16.84 K
Method-2	19.48 K ± 15.97 K	15.01 K ± 15.83 K	25.76 K ± 16.7 K	15.99 K ± 16.26 K	20.11 K ± 16.28 K

Note. The mean temperature differences and corresponding standard deviations are shown for each set of Einstein coefficients.

Therefore, it is very unlikely that a single fixed peak altitude and fixed FWHM VER (e.g., a single SABER 1.6 μm or a single Gaussian VER) could truly represent the OH(6,2) band VER for the entire night. In addition, it is now well understood that different vibrational bands of the OH emission have different peak emission altitudes (von Savigny et al., 2012; Xu et al., 2012). As per these reports, the peak of the OH(6,2) band VER should be located at a slightly higher altitude in comparison to the SABER 1.6 μm VER peak altitude. Therefore, the weighting functions used in this analysis appear to be an important controlling factor of the temperature difference.

The choice of Einstein transition coefficients for the P1 rotational lines also could lead to some degree of ambiguity in the EFS temperature estimation. To derive all the rotational temperatures shown in the previous sections, we have adopted the Einstein coefficients prescribed by Langhoff et al. (1986). To examine the dependence of rotational temperatures on the Einstein coefficients, we are now considering five sets of well-known coefficients. We shall be referring to these different sets of coefficients by using their abbreviated names as, Mies (Mies, 1974), LWR (Langhoff et al., 1986), TL (Turnbull & Lowe, 1989), Loo (van der Loo & Groenenboom, 2007, 2008), and Hitran (Goldman et al., 1998; Rothman et al., 2009). We have estimated the mean temperature difference between the EFS and K-Lidar temperatures using both method-1 and method-2 and applying these five sets of Einstein coefficients. The results are summarized in Table 4 which shows that rotational temperature estimation depends strongly on the choice of the Einstein coefficients. In our study the order of mean temperature differences (ΔT) turns out to be ΔT (LWR) < ΔT (Loo) < ΔT (Mies) < ΔT (Hitran) < ΔT (TL), which conform to the findings of Liu et al. (2015) and Phillips et al. (2004). Therefore, we decided to utilize rotational temperatures derived by using the LWR coefficients for the rest of the study.

On the other hand, the FoV of the EFS, K-Lidar, and SABER are very different. Therefore, the assumption that the airglow intensity and temperature field are uniform over all these three FoVs may not essentially be correct, especially in the MLT region, which is very dynamic at all times. Atmospheric waves of different scales are omnipresent in the MLT region and many of these waves have horizontal scale sizes of ∼10s km. These waves could partially or fully cover the FoV of the EFS and cause an advection of air masses having different temperatures which could contribute to the temperature bias between EFS and K-Lidar (von Zahn et al., 1987). We have also noted temperature differences of 2–5 K between successive passes of SABER (Table 3), which clearly shows that strong variabilities are present in the MLT region even within a small area of ±2.5° latitude-longitude. She and Lowe (1998) have mentioned that the OH band intensity varies non-linearly with the temperature. Therefore, the direct application of a weighting function that mimics the OH VER on a Lidar temperature profile may lead to a discrepancy of a few K in the weighted Lidar temperatures. In this work, we have studied the effects of variabilities in the peak altitudes and FWHMs of the OH(6,2) VER on the EFS and K-Lidar temperature comparison in detail.

4.2. Investigation of OH(6,2) Band Peak Altitude and FWHM Variation

4.2.1. Study of OH(6,2) Band VER Peak Altitudes During February-April 2005

We have investigated variations in the OH(6,2) band VER peak altitudes with local time during February–April 2005 by using two different techniques as described below. Both these techniques use observed SABER OH VER data. Alternately, one could also study variations in the OH(6,2) band VER parameters by using model equations as prescribed by McDade et al. (1987), Grygalashvyly et al. (2014), etc.

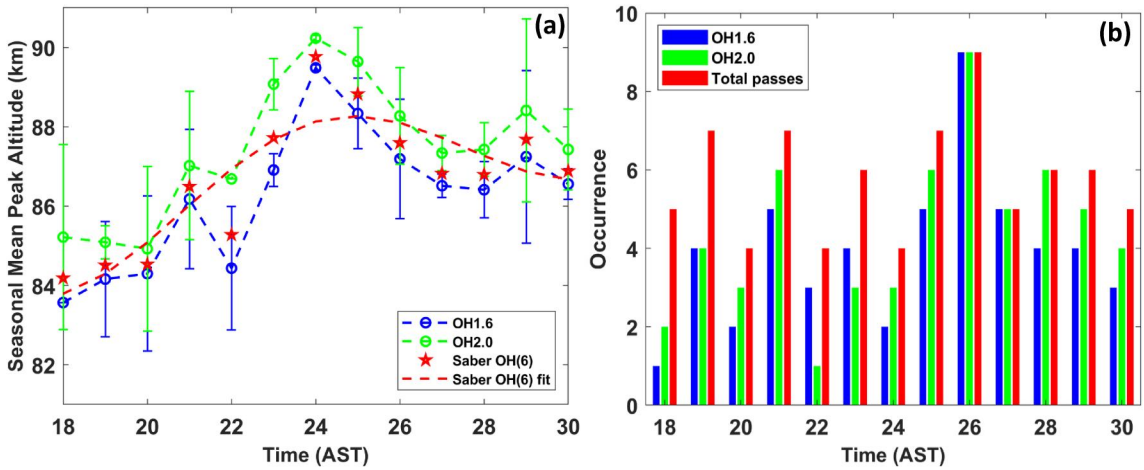

Figure 9. (a) Temporal variation of SMPAs of the SABER 1.6 and 2.0 μm VER are shown in blue and green color open circles, respectively, along with their corresponding standard deviations. SMPAs and LTT of the OH*(6) level are depicted by red stars and a red dotted line, respectively. (b) The occurrence of the single peak SABER 1.6 and 2.0 μm VER profiles along with the total number of SABER passes within each 1-hr time bin during our study period are shown here.

4.2.1.1. Estimation of OH(6,2) Band VER Peak Altitudes by Using SABER Observations

Both the SABER 1.6 and 2.0 μm *ch.* do not measure the OH(6,2) band directly. Therefore, we have adapted the method suggested by Liu et al. (2015) to derive peak altitudes of the OH*(6) level using these two SABER *ch.* data. The VER of the OH(6,2) band is expected to have the same peak altitude and FWHM as the OH*(6) level since, OH(6,2) = A (6,2) × OH*(6) where, A (6,2) represents the average Einstein transition coefficient between $v' = 6$ and $v' = 2$ vibrational levels. This method assumes that peak altitudes of different OH vibrational levels are equally spaced in altitude, and the higher vibrational levels have their peaks at higher altitudes (von Savigny et al., 2012; Xu et al., 2012). In this analysis, all the SABER passes available between 01 February 2005 and 30 April 2005 within the area of the AO ± 2.5° latitude-longitude during the nighttime (18:00–30:00 AST) are considered irrespective of the availability of EFS and K-Lidar data. Peak altitudes of the SABER 1.6 and 2.0 μm VER are considered when there is only one peak within the half maxima of the peak VER. To obtain the seasonal mean peak altitude (SMPA) of the two SABER channels at any particular time, all the peak altitudes available within the ±30 min interval of that time are averaged. The SMPAs of the two channels of SABER and the OH (6,2) band during nighttime are shown in Figure 9a. The number of SABER VER profiles or SABER passes available within a 1-hr time bin during the whole study period is defined as their occurrence. The Occurrence of single peak VER of the two SABER *ch.* during nighttime is presented in Figure 9b. Occurrences are not uniform in all the time bins (Figure 9b), and this could cause a bias in the SMPAs of the OH(6,2) band at certain hours. Thus, to obtain the local time trend (LTT) of the OH(6,2) peak altitudes, a sixth-order polynomial is fitted to the OH(6,2) SMPAs between 15:00 AST and 33:00 AST. An additional 3 hr are considered on both sides of the 18:00–30:00 AST window to avoid edge effects of the fitting process.

4.2.1.2. Estimation of the OH(6,2) Band VER Peak Altitudes Using an Analytical Model Generated From SABER Data

In this methodology, all the single peak SABER 1.6 and 2.0 μm VER profiles over AO ± 2.5° latitude-longitude between 01 February 2005 and 30 April 2005 are considered. Considering both day and night time, there are 102 passes of SABER over AO during this period; out of which 60 (~59%) and 74 (~73%) passes contain single peak profiles in the 1.6 and 2.0 μm *ch.*, respectively. All these single peak profiles are decomposed into two Gaussian components following the method described in Section 3.2. Area, peak altitude, and FWHM corresponding to the two sets of Gaussians are fitted with a six-degree polynomial to find out their temporal variations following the criteria described by Santos et al. (2022). The model OH 1.6 μm and 2.0 μm VER at any time is calculated by using the area, peak altitude, and FWHM provided by their respective polynomial fits at that time. Peak altitudes of the model OH(6,2) VER are estimated from the model OH 1.6 μm and 2.0 μm VER peak altitudes by using the same technique as described in Section 4.2.1.1. Since all these peak altitudes are based on the polynomial-fitted

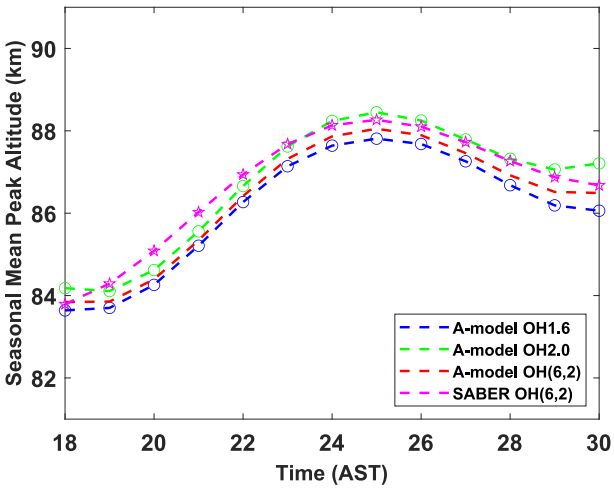

Figure 10. Temporal variation of SMPAs of the SABER 1.6 and 2.0 μm VER provided by the A-model are shown in blue and green color open circles, respectively. LTT of the OH(6,2) band peak altitudes obtained by using the A-model and SABER observation are represented by red and magenta dotted lines, respectively. The SABER OH(6,2) LTT shown here and the SABER OH(6) fit shown by the red dotted line in Figure 9(a) are the same.

Gaussian parameters, they are expected to represent their seasonal mean values. The analytical method used in this section to obtain SMPAs will be hereafter referred to as the "A-model." The analysis results are shown in Figure 10.

4.2.1.3. Comparison Between OH(6,2) Band VER Peak Altitudes Obtained in This Work and Previous Studies

The LTT of SABER and A-model derived peak altitudes match quite well throughout the night with the A-model values being 0.2–0.7 km smaller than the SABER values (Figure 10). SMPAs obtained from SABER and A-model exhibit an increasing trend until midnight and a decreasing trend after midnight. Takahashi et al. (2005) have reported a similar temporal variation in the OH(6,2) band peak altitudes from Shigaraki, Japan (35°N, 136°E), as has been obtained in this work. They observed that the highest peak altitude occurred between 22:00 local time (LT) and 23:00 LT, which is about 2 hr earlier in comparison to our SABER SMPAs. Zhao et al. (2005) studied the temporal trend of the OH(6,2) band peak altitudes from Maui, Hawaii (20.8° N, 156.2°W). They reported a monotonically decreasing trend which is contrary (similar) to the SABER and A-model results before (after) midnight, although the slope of the trend is much larger in their study. One potential factor for different temporal trends at different locations could be the variable latitude and longitude dependence of the peak altitudes. Also, the solar activity level is different during the study period of our work and the other two works (F10.7 = 150 to 270 for Zhao et al. (2005); F10.7 = 120 to 140 for Takahashi et al. (2005); F10.7 = 70 to 120 for the present study). Since the background atmosphere varies with the solar activity level, the wave and tidal influence on the atmosphere might differ during the period of all these three works. However, a detailed study with more data is required to understand the underlying causes of such variations.

4.2.2. Study of OH(6,2) Band VER FWHM During February-April 2005

The FWHM of the OH(6,2) VER is studied by applying the same techniques used in Section 4.2.1 to estimate peak altitudes of the OH(6,2) VER. In the first method, the seasonal mean FWHM (SMFWHM) of the two channels of SABER is obtained by using the same methodology which is applied to derive the SMPAs of these two channels in Section 4.2.1.1. The exact relation of the OH(6,2) VER FWHM to the SABER 1.6 and 2.0 μm VER FWHM is unknown. Therefore, the average of SMFWHMs obtained from the two channels of SABER is assumed to represent SMFWHMs of the OH(6,2) band VER. In the second method, SMFWHMs of the OH(6,2) band are estimated by averaging the SMFWHMs of the SABER 1.6 and 2.0 μm ch. VER obtained from the A-model. Sixth-order polynomials are fitted to the OH(6,2) band SMFWHMs provided by these two methods to obtain their respective LTT. SMFWHM values obtained by using these methods are depicted in Figure 11.

The LTT of the SABER-derived OH(6,2) band FWHM shows an increasing trend in the evening hours followed by a gradually decreasing trend for the rest of the night. A peak is observed in the SABER-derived FWHM LTT at ~21:00 AST (Figure 11a). The A-model derived OH(6,2) band SMFWHMs show an increasing trend in the evening hours followed by a sharply decreasing trend which again reverses in the early morning hours (Figure 11b). This temporal behavior is very different than the SABER FWHM LTT. The A-model derived SMFWHMs of the OH(6,2) band are comparable with the SABER-derived values during the evening and early morning hours only, and at other times, differences of 1–1.5 km are observed between them. The whole night average of the SMFWHMs derived from SABER observation and A-model turns out to be 7.28 ± 0.92 km and 7.97 ± 0.97 km, respectively. Therefore, the average SMFWHM obtained from SABER observation and the A-model match well with the average FWHM reported by Baker and Stair (1988). To our knowledge, this is the first work to discuss the local time variation of the OH band FWHM in detail.

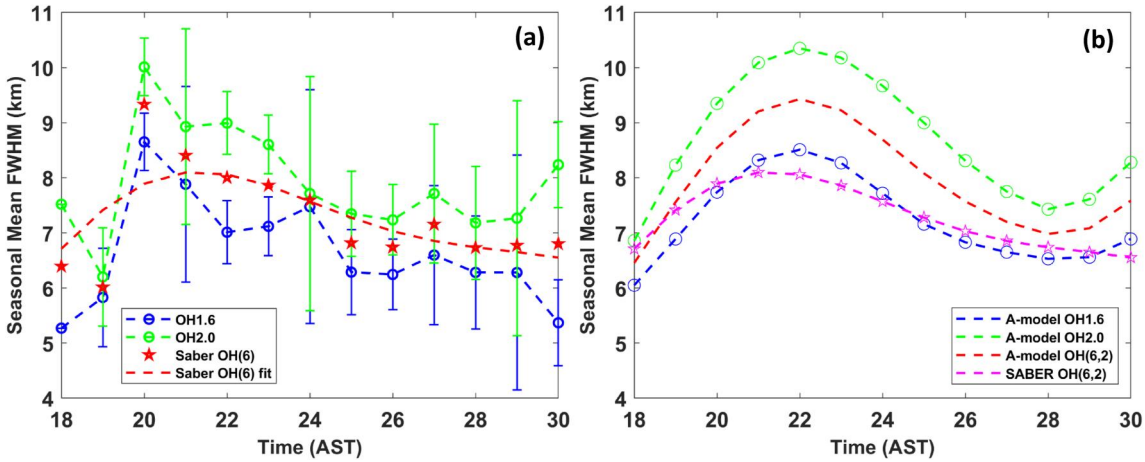

Figure 11. (a) SMFWHMs of the SABER 1.6 and 2.0 μm are shown in blue and green color open circles, respectively, along with their corresponding standard deviations. SABER-derived SMFWHMs of the OH(6,2) band and their LTT are represented by red stars and a red dotted line, respectively. (b) SMFWHMs of the SABER 1.6 and 2.0 μm ch. obtained by using the A-model are depicted by blue and green color open circles, respectively. LTT of the OH(6,2) band FWHMs obtained from the A-model and SABER observations are represented by red and magenta dotted lines, respectively. The SABER OH(6,2) FWHM LTT shown in this panel and the SABER OH(6) fit shown in panel (a) of this figure are the same.

4.3. Comparison Between EFS and K-Lidar Temperatures Using a Time-Varying Weighting Function

It is evident from Figures 9a and 11a that there are significant temporal variations in the SMPAs and SMFWHMs of the OH (6,2) band. It is quite possible that larger temporal variabilities may occur in these two parameters on a day-to-day basis. These results also indicate that a single SABER OH VER profile or a single Gaussian function is not the best representation of the OH VER profiles for the whole night. Therefore, we reanalyzed the EFS and K-Lidar temperature differences by using two different methods, which utilize time-varying peak altitudes and FWHMs of the OH(6,2) band. In one method, Gaussian functions are used as weighting functions. The peak altitudes and FWHMs for the Gaussians are adopted from the LTT of the SABER-derived OH(6,2) band peak altitude and FWHM, respectively. The minimum weight factor limit and the selection criteria of the K-Lidar temperature profiles are the same as has been described in Section 3.2. The mean temperature difference between the EFS and K-Lidar is determined in the same way as mentioned in Section 4.1.1. We shall henceforth refer to this weighting method as "method-3."

In the other method, we have considered the OH 1.6 μm VER profiles provided by the A-model at 1-hr intervals during 18:00–30:00 AST. Peak altitudes and FWHMs of the OH 1.6 μm VER profiles are modified with the LTT

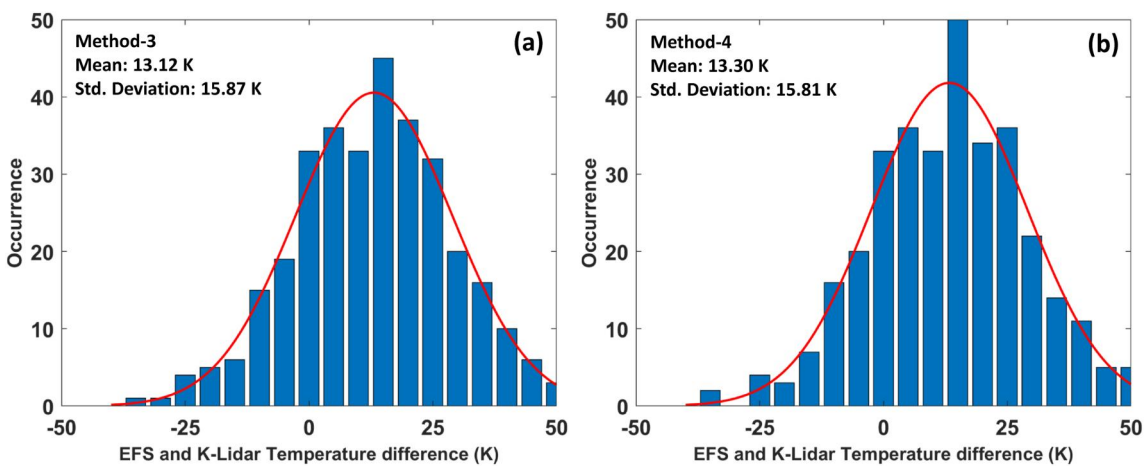

Figure 12. Distribution of EFS and weighted K-Lidar temperature differences during February–April 2005 obtained by using (a) method-3 and (b) method-4. The remaining properties of the Figure are the same as in Figure 8.

of the corresponding parameters for the OH(6,2) band obtained from the A-model. The application of the resulting OH(6,2) band VERs to weight the K-Lidar temperature profiles is termed "method-4." All the remaining criteria are the same for method-3 and method-4. Since the A-model derived OH 1.6 μm VER is composed of two Gaussians, it is quite difficult to reproduce the FWHM of the OH(6,2) VER with 100% accuracy. In our computation, we are able to achieve 93%–97% accuracy. Considering the average FWHM of ∼8 km for the A-model derived OH(6,2) band and altitude resolution of 0.45 km of the K-Lidar, the effects of this small discrepancy should be negligible in the weighted K-Lidar temperatures. This problem is not encountered while reproducing the peak altitudes of the A-model derived OH(6,2) VER.

The mean temperature difference between EFS and K-Lidar is found to be marginally better for method-3 in comparison to method-4 while standard deviations are comparable for both methods (Figure 12). In the case of method-3, it is observed that there are 42.24%, 58.07%, and 71.12% points within the temperature difference range of ±10 K, ±15 K, and ±20 K, respectively. For method-4, the corresponding values are 41.69%, 58.91%, and 70.09%, respectively, which are identical to method-3. Therefore, method-3 and method-4 produce similar comparisons between EFS and K-lidar temperatures though the shape of the weighting functions were different in these two methods. It is discussed in Section 4.1.5 that FWHMs of the OH(6,2) band also play an important role in this comparison process aside from the peak altitudes. It could be possible that the differences in peak altitudes (Figure 10) and FWHMs (Figure 11b) between method-3 and method-4 have compensated for the effects of the shape of the weighting functions.

By comparing the results shown in Figures 8 and 12, it is observed that the mean temperature difference obtained by method-3 is 1.13 K smaller than that by method-1. Similarly, method-4 provides a mean temperature difference that is 1.71 K smaller in comparison to method-2. The standard deviation has improved slightly for method-3 over method-1, while it is almost the same for method-2 and method-4. On the other hand, there is a slight improvement in the percentage of points within the temperature difference of ±10 K, ±15 K, and ±20 K for method-3 and method-4 over method-1 and method-2. All these results show that the use of time-varying peak altitudes and FWHMs provides a better comparison between EFS and K-Lidar temperatures instead of using a single weighting function of fixed peak altitude and fixed FWHM for the whole night. Further, our analysis indicates that statistically, Gaussian weighting functions provide similar outcomes in comparison to weighting functions that resemble the SABER OH VERs. The SMPAs, SMFWHMs, and LTT of the OH(6,2) VER could be improved by considering a larger satellite database. Also, a larger database could help to understand the solar activity level and seasonal dependence of these parameters in more detail and improve the time resolution of these seasonal mean parameters. Even though the LTTs may not exactly replicate the actual magnitude of these parameters on a day-to-day basis, it is the second-best available option that could significantly improve the inter-comparison of altitude-resolved and altitude-integrated measurements.

5. Summary and Conclusion

In this work, we have discussed in detail the analysis methodology adopted to retrieve rotational temperatures in the MLT region from the AO EFS OH(6,2) Meinel band spectra. The results are validated by inter-comparison between the AO EFS, AO K-Lidar, and SABER temperatures for the period of February–April 2005. Four different methods are adapted to weight the K-Lidar temperature profiles. In the first and second methods (method-1 and method-2), a single weighting function is used for the whole night. The third and fourth methods (method-3 and method-4) are based on weighting functions that utilize time-varying peak altitudes and FWHMs of the OH(6,2) band. Temporal variation of the OH(6,2) band peak altitudes and FWHMs are investigated by using direct observation of the 1.6 and 2.0 μm VER profiles by SABER and an analytical model based on the SABER 1.6 and 2.0 μm VER profiles (A-model).

The main findings of this study are noted below.

1. Inter-comparison between altitude-resolved and altitude-integrated temperature measurements improves when a weighting function that utilizes time-varying peak altitudes and FWHMs is used instead of a weighting function that has fixed peak altitude and fixed FWHM for the whole night. In this work, the mean temperature difference between the EFS and K-Lidar decreases by ∼1.1–1.7 K when applying time-varying weighting functions instead of fixed weighting functions.
2. By applying time-varying weighting functions, the mean temperature difference between the AO EFS and K-Lidar is found to be ∼13 K during our study period. Comparison between simultaneous SABER, EFS, and K-

Lidar temperatures results in an average temperature difference of ∼9 K between EFS and K-Lidar. These results are comparable with the findings reported in the previous studies from different locations.

3. It is found that rotational temperature estimation from the EFS data depends strongly on the choice of Einstein transition coefficients for the P1 rotational lines of the OH(6,2) band. In this study, the mean temperature difference between EFS and K-Lidar by using different Einstein transition coefficients turns out to be in the following order, ΔT (LWR) < ΔT (Loo) < ΔT (Mies) < ΔT (Hitran) < ΔT (TL).
4. The LTT of the OH(6,2) band peak altitudes and FWHMs estimated by using the SABER 1.6 and 2.0 μm VER profiles show that there are considerable temporal variabilities in these two parameters during the study period. SMPAs obtained from SABER observations and the A-model are found to be similar while significant discrepancies are noticed in the SMFWHMs obtained from these two methods.
5. We observed that statistically Gaussian weighting functions and weighting functions that resemble the shape of SABER OH VERs, provide similar mean temperature differences between the EFS and K-Lidar.

Data Availability Statement

The AO EFS raw data, EFS rotational temperatures, and AO K-Lidar temperature data (Sau et al., 2024) are available on https://doi.org/10.5281/zenodo.10608517. Boston University all-sky imager data can be accessed from http://sirius.bu.edu/dataview/. The SABER data is available from http://saber.gats-inc.com/browse_data.php#.

Acknowledgments
This work was mainly carried out at AO when SS, PT, CGMB, and JL were working there in different positions. AO was operated by the University of Central Florida (UCF) during 2018–2023 under a cooperative agreement with the National Science Foundation (AST-1744119) and in alliance with Yang Enterprises and Ana G. Méndez-Universidad Metropolitana. SS was supported by the UCF Preeminent Postdoctoral Program (P3). CGMB, PT, and JL would like to thank the support from the NSF Award AGS-2221770. Research at the Indian Institute of Geomagnetism is funded by the Department of Science and Technology (DST), Government of India. We wish to thank the whole TIMED mission team for making the SABER data publicly available. We thank Dr. Robert B. Kerr of Computational Physics Inc., Lowell, MA, USA for all the valuable discussions and suggestions during this work. We thank all the anonymous reviewers for their valuable suggestions that helped to improve the quality of this work.

References

Baker, D. J., & Stair, A. T., Jr. (1988). Rocket measurements of the altitude distributions of the hydroxyl airglow. *Physica Scripta*, *37*(4), 611–622. https://doi.org/10.1088/0031-8949/37/4/021

Bittner, M., Offermann, D., Graef, H. H., Donner, M., & Hamilton, K. (2002). An 18-year time series of OH rotational temperatures and middle atmosphere decadal variations. *Journal of Atmospheric and Solar-Terrestrial Physics*, *64*(8), 1147–1166. https://doi.org/10.1016/S1364-6826(02)00065-2

Burns, G. B., Kawahara, T. D., French, W. J. R., Nomura, A., & Klekociuk, A. R. (2003). A comparison of hydroxyl rotational temperatures from Davis (69°S, 78°E) with sodium lidar temperatures from Syowa (69°S, 39°E). *Geophysical Research Letters*, *30*(1). https://doi.org/10.1029/2002GL016413

Burnside, R. G., Meriwether, J. W., Jr., & Walker, J. C. G. (1980). Airglow observations of the OI 7774 Å multiplet at Arecibo during a magnetic storm. *Journal of Geophysical Research*, *85*(A2), 767–773. https://doi.org/10.1029/JA085iA02p00767

Burnside, R. G., Meriwether, J. W., & Torr, M. R. (1977). Contamination of ground-based measurements of OI (6300 Å) and NI (5200 Å) airglow by OH emissions. *Planetary and Space Science*, *25*(10), 985–988. https://doi.org/10.1016/0032-0633(77)90012-5

Dunker, T. (2018). The airglow layer emission altitude cannot be determined unambiguously from temperature comparison with lidars. *Atmospheric Chemistry and Physics*, *18*(9), 6691–6697. https://doi.org/10.5194/acp-18-6691-2018

Esplin, R., Mlynczak, M. G., Russell, J., Gordley, L., & Team, T. S. (2023). Sounding of the Atmosphere using Broadband Emission Radiometry (SABER): Instrument and science measurement description. *Earth and Space Science*, *10*(9), e2023EA002999. https://doi.org/10.1029/2023EA002999

Fricke, K. H., & von Zahn, U. (1985). Mesopause temperatures derived from probing the hyperfine structure of the D2 resonance line of sodium by lidar. *Journal of Atmospheric and Terrestrial Physics*, *47*(5), 499–512. https://doi.org/10.1016/0021-9169(85)90116-3

Friedman, J. S. (2003). Tropical mesopause climatology over the Arecibo observatory. *Geophysical Research Letters*, *30*(12). https://doi.org/10.1029/2003GL016966

Friedman, J. S., & Chu, X. (2007). Nocturnal temperature structure in the mesopause region over the Arecibo Observatory (18.35°N, 66.75°W): Seasonal variations. *Journal of Geophysical Research*, *112*(D14). https://doi.org/10.1029/2006JD008220

Friedman, J. S., Tepley, C. A., Raizada, S., Zhou, Q. H., Hedin, J., & Delgado, R. (2003). Potassium Doppler-resonance lidar for the study of the mesosphere and lower thermosphere at the Arecibo Observatory. *Journal of Atmospheric and Solar-Terrestrial Physics*, *65*(16), 1411–1424. https://doi.org/10.1016/j.jastp.2003.09.004

García-Comas, M., López-Puertas, M., Marshall, B. T., Wintersteiner, P. P., Funke, B., Bermejo-Pantaleón, D., et al. (2008). Errors in Sounding of the Atmosphere using Broadband Emission Radiometry (SABER) kinetic temperature caused by non-local-thermodynamic-equilibrium model parameters. *Journal of Geophysical Research*, *113*(D24). https://doi.org/10.1029/2008JD010105

Goldman, A., Schoenfeld, W. G., Goorvitch, D., Chackerian, C., Dothe, H., Mélen, F., et al. (1998). Updated line parameters for OH X2II–X2II (v'',v') transitions. *Journal of Quantitative Spectroscopy and Radiative Transfer*, *59*(3), 453–469. https://doi.org/10.1016/S0022-4073(97)00112-X

Grygalashvyly, M., Sonnemann, G. R., Lübken, F.-J., Hartogh, P., & Berger, U. (2014). Hydroxyl layer: Mean state and trends at midlatitudes. *Journal of Geophysical Research: Atmospheres*, *119*(21), 12391–312419. https://doi.org/10.1002/2014JD022094

Hecht, J. H., Kane, T. J., Walterscheid, R. L., Gardner, C. S., & Teplky, C. A. (1993). Simultaneous nightglow and Na lidar observations at Arecibo during the AIDA-89 campaign. *Journal of Atmospheric and Terrestrial Physics*, *55*(3), 409–423. https://doi.org/10.1016/0021-9169(93)90077-C

Hocking, W. K. (1999). Temperatures Using radar-meteor decay times. *Geophysical Research Letters*, *26*(21), 3297–3300. https://doi.org/10.1029/1999GL003618

Höffner, J., & Lautenbach, J. (2009). Daylight measurements of mesopause temperature and vertical wind with the mobile scanning iron lidar. *Optics Letters*, *34*(9), 1351–1353. https://doi.org/10.1364/OL.34.001351

Holmen, S. E., Dyrland, M. E., & Sigernes, F. (2014). Long-term trends and the effect of solar cycle variations on mesospheric winter temperatures over Longyearbyen, Svalbard (78°N). *Journal of Geophysical Research: Atmospheres*, *119*(11), 6596–6608. https://doi.org/10.1002/2013JD021195

Kane, T. J., Gardner, C. S., Znou, Q., Mathews, J. D., & Tepley, C. A. (1993). Lidar, radar and airglow observations of a prominent sporadic Na/sporadic E layer event at Arecibo during AIDA-89. *Journal of Atmospheric and Terrestrial Physics*, *55*(3), 499–511. https://doi.org/10.1016/0021-9169(93)90084-C

Kerr, R. B., Garcia, R., He, X., Noto, J., Lancaster, R. S., Tepley, C. A., et al. (2001). Periodic variations of geocoronal Balmer-alpha brightness due to solar-driven exospheric abundance variations. *Journal of Geophysical Research*, *106*(A12), 28797–28817. https://doi.org/10.1029/1999JA900186

Krassovsky, V. I., Shefov, N. N., & Yarin, V. I. (1962). Atlas of the airglow spectrum 3,000–12,400 Å. *Planetary and Space Science*, *9*(12), 883–915. https://doi.org/10.1016/0032-0633(62)90008-9

Langhoff, S. R., Werner, H. J., & Rosmus, P. (1986). Theoretical transition probabilities for the OH meinel system. *Journal of Molecular Spectroscopy*, *118*(2), 507–529. https://doi.org/10.1016/0022-2852(86)90186-4

Liu, W., Xu, J., Smith, A. K., & Yuan, W. (2015). Comparison of rotational temperature derived from ground-based OH airglow observations with TIMED/SABER to evaluate the Einstein coefficients. *Journal of Geophysical Research: Space Physics*, *120*(11), 10069–10082. https://doi.org/10.1002/2015JA021886

Lübken, F.-J. (1999). Thermal structure of the Arctic summer mesosphere. *Journal of Geophysical Research*, *104*(D8), 9135–9149. https://doi.org/10.1029/1999JD900076

McDade, I. C., Llewellyn, E. J., Murtagh, D. P., & Greer, R. G. H. (1987). Eton 5: Simultaneous rocket measurements of the OH meinel $\Delta\upsilon = 2$ sequence and (8,3) band emission profiles in the nightglow. *Planetary and Space Science*, *35*(9), 1137–1147. https://doi.org/10.1016/0032-0633(87)90020-1

Meinel, A. B. (1950). OH emission bands in the spectrum of the night sky. *The Astrophysical Journal*, *111*, 555–564. https://doi.org/10.1086/145296

Meriwether, J. W. (1979). Measurement of weak airglow emissions with a programmable scanning spectrometer. *Planetary and Space Science*, *27*(10), 1221–1232. https://doi.org/10.1016/0032-0633(79)90101-6

Meriwether, J. W., Jr., Torr, D. G., Walker, J. C. G., & Nier, A. O. (1978). The O+(^{2}P) emission at 7320 Å in twilight. *Journal of Geophysical Research*, *83*(A7), 3311–3319. https://doi.org/10.1029/JA083iA07p03311

Meriwether, J. W. J. W., Jr., & Walker, J. C. G. (1977). Intensity of the first negative band system of nitrogen in the night sky over Arecibo. *Journal of Geophysical Research*, *82*(13), 1855–1858. https://doi.org/10.1029/JA082i013p01855

Mies, F. H. (1974). Calculated vibrational transition probabilities of OH(X2Π). *Journal of Molecular Spectroscopy*, *53*(2), 150–188. https://doi.org/10.1016/0022-2852(74)90125-8

Mulligan, F. J., Dyrland, M. E., Sigernes, F., & Deehr, C. S. (2009). Inferring hydroxyl layer peak heights from ground-based measurements of OH(6-2) band integrated emission rate at Longyearbyen (78°N, 16°E). *Annals of Geophysics*, *27*(11), 4197–4205. https://doi.org/10.5194/angeo-27-4197-2009

Myrabø, H. K., Romick, G. J., Sivjee, G. G., & Deehr, C. S. (1984). Night airglow OH (8–3) band rotational temperatures at Poker Flat, Alaska. *Journal of Geophysical Research*, *89*(A10), 9153–9156. https://doi.org/10.1029/JA089iA10p09153

Nordberg, W., Katchen, L., Theon, J., & Smith, W. S. (1965). Rocket observations of the structure of the mesosphere. *Journal of the Atmospheric Sciences*, *22*(6), 611–622. https://doi.org/10.1175/1520-0469(1965)022<0611:rootso>2.0.co;2

Pendleton, W. R., Jr., Espy, P. J., & Hammond, M. R. (1993). Evidence for non-local-thermodynamic-equilibrium rotation in the OH nightglow. *Journal of Geophysical Research*, *98*(A7), 11567–11579. https://doi.org/10.1029/93JA00740

Phillips, F., Burns, G. B., French, W. J. R., Williams, P. F. B., Klekociuk, A. R., & Lowe, R. P. (2004). Determining rotational temperatures from the OH(8-3) band, and a comparison with OH(6-2) rotational temperatures at Davis, Antarctica. *Annals of Geophysics*, *22*(5), 1549–1561. https://doi.org/10.5194/angeo-22-1549-2004

Rothman, L. S., Gordon, I. E., Barbe, A., Benner, D. C., Bernath, P. F., Birk, M., et al. (2009). The HITRAN 2008 molecular spectroscopic database. *Journal of Quantitative Spectroscopy and Radiative Transfer*, *110*(9), 533–572. https://doi.org/10.1016/j.jqsrt.2009.02.013

Russell, J., Mlynczak, M., & Gordley, L. (1994). *Overview of the sounding of the Atmosphere using Broadband Emission Radiometry (SABER) experiment for the Thermosphere-Ionsphere-Mesosphere Energetics and Dynamics (TIMED) mission* (Vol. 2266). SPIE.

Santos, Â. M., Brum, C. G. M., Batista, I. S., Sobral, J. H. A., Abdu, M. A., & Souza, J. R. (2022). Responses of intermediate layers to geomagnetic activity during the 2009 deep solar minimum over the Brazilian low-latitude sector. *Annals of Geophysics*, *40*(3), 259–269. https://doi.org/10.5194/angeo-40-259-2022

Sau, S., Terra, P., Brum, C. G. M., Vargas, F. A., Lautenbach, J., & Gurubaran, S. (2024). Data for: Retrieval of rotational temperatures from the Arecibo Observatory Ebert-Fastie spectrometer and their inter-comparison with co-located K-Lidar and SABER measurements. *Zenodo*. https://doi.org/10.5281/zenodo.10608517

She, C. Y., & Lowe, R. P. (1998). Seasonal temperature variations in the mesopause region at mid-latitude: Comparison of lidar and hydroxyl rotational temperatures using windii\uars oh height profiles. *Journal of Atmospheric and Solar-Terrestrial Physics*, *60*(16), 1573–1583. https://doi.org/10.1016/S1364-6826(98)00082-0

She, C. Y., & Yu, J. R. (1994). Simultaneous three-frequency Na lidar measurements of radial wind and temperature in the mesopause region. *Geophysical Research Letters*, *21*(17), 1771–1774. https://doi.org/10.1029/94GL01417

Sigernes, F., Holmes, J. M., Dyrland, M., Lorentzen, D. A., Chernous, S. A., Svinyu, T., et al. (2007). Absolute calibration of optical devices with a small field of view. *Journal of Optical Technology*, *74*(10), 669–674. https://doi.org/10.1364/JOT.74.000669

Sigernes, F., Shumilov, N., Deehr, C. S., Nielsen, K. P., Svenøe, T., & Havnes, O. (2003). Hydroxyl rotational temperature record from the auroral station in Adventdalen, Svalbard (78°N, 15°E). *Journal of Geophysical Research*, *108*(A9). https://doi.org/10.1029/2001JA009023

Sivjee, G. G., Dick, K. A., & Feldman, P. D. (1972). Temporal variations in night-time hydroxyl rotational temperature. *Planetary and Space Science*, *20*(2), 261–269. https://doi.org/10.1016/0032-0633(72)90107-9

Takahashi, H., Wrasse, C. M., Gobbi, D., Nakamura, T., Shiokawa, K., & Lima, L. M. (2005). Airglow OH emission height inferred from the OH temperature and meteor trail diffusion coefficient. *Advances in Space Research*, *35*(11), 1940–1944. https://doi.org/10.1016/j.asr.2005.05.052

Tepley, C. A., & Mathews, J. D. (1978). Preliminary measurements of ion-neutral collision frequencies and mean temperatures in the Arecibo 80- to 100-km altitude region. *Journal of Geophysical Research*, *83*(A7), 3299–3302. https://doi.org/10.1029/JA083iA07p03299

Tepley, C. A., Mathews, J. D., Meriwether, J. W., Jr., & Walker, J. C. G. (1981). Observations of the Ca+ twilight airglow from intermediate layers of ionization. *Journal of Geophysical Research*, *86*(A9), 7781–7786. https://doi.org/10.1029/JA086iA09p07781

Turnbull, D. N., & Lowe, R. P. (1989). New hydroxyl transition probabilities and their importance in airglow studies. *Planetary and Space Science*, *37*(6), 723–738. https://doi.org/10.1016/0032-0633(89)90042-1

van der Loo, M. P. J., & Groenenboom, G. C. (2007). Theoretical transition probabilities for the OH Meinel system. *The Journal of Chemical Physics*, *126*(11), 114314–114500. https://doi.org/10.1063/1.2646859

van der Loo, M. P. J., & Groenenboom, G. C. (2008). Theoretical transition probabilities for the OH Meinel system. *The Journal of Chemical Physics*, *128*(15), 159902. https://doi.org/10.1063/1.2899016

Vargas, F. (2019). Uncertainties in gravity wave parameters, momentum fluxes, and flux divergences estimated from multi-layer measurements of mesospheric nightglow layers. *Advances in Space Research*, *63*(2), 967–985. https://doi.org/10.1016/j.asr.2018.09.039

Vargas, F., Chau, J. L., Charuvil Asokan, H., & Gerding, M. (2021). Mesospheric gravity wave activity estimated via airglow imagery, multistatic meteor radar, and SABER data taken during the SIMONe–2018 campaign. *Atmospheric Chemistry and Physics*, *21*(17), 13631–13654. https://doi.org/10.5194/acp-21-13631-2021

von Savigny, C., McDade, I. C., Eichmann, K. U., & Burrows, J. P. (2012). On the dependence of the OH* Meinel emission altitude on vibrational level: SCIAMACHY observations and model simulations. *Atmospheric Chemistry and Physics*, *12*(18), 8813–8828. https://doi.org/10.5194/acp-12-8813-2012

von Zahn, U., Fricke, K. H., Gerndt, R., & Blix, T. (1987). Mesospheric temperatures and the OH layer height as derived from ground-based lidar and OH∗ spectrometry. *Journal of Atmospheric and Terrestrial Physics*, *49*(7), 863–869. https://doi.org/10.1016/0021-9169(87)90025-0

Walterscheid, R. L., Hecht, J. H., Djuth, F. T., & Tepley, C. A. (2000). Evidence of reflection of a long-period gravity wave in observations of the nightglow over Arecibo on May 8–9, 1989. *Journal of Geophysical Research*, *105*(D5), 6927–6934. https://doi.org/10.1029/1999JD901065

Xu, J., Gao, H., Smith, A. K., & Zhu, Y. (2012). Using TIMED/SABER nightglow observations to investigate hydroxyl emission mechanisms in the mesopause region. *Journal of Geophysical Research*, *117*(D2). https://doi.org/10.1029/2011JD016342

Yu, J. R., Latifi, H., She, C. Y., Yee, J. H., & Niciejewski, R. J. (1991). Simultaneous lidar and airglow temperature measurements in the mesopause region. *Geophysical Research Letters*, *18*(7), 1361–1363. https://doi.org/10.1029/91GL01153

Zhao, Y., Taylor, M. J., & Chu, X. (2005). Comparison of simultaneous Na lidar and mesospheric nightglow temperature measurements and the effects of tides on the emission layer heights. *Journal of Geophysical Research*, *110*(D9). https://doi.org/10.1029/2004JD005115

Zhou, Q. H., Sulzer, M. P., Tepley, C. A., Fesen, C. G., Roble, R. G., & Kelley, M. C. (1997). Neutral winds and temperature in the tropical mesosphere and lower thermosphere during January 1993: Observation and comparison with TIME-GCM results. *Journal of Geophysical Research*, *102*(A6), 11507–11519. https://doi.org/10.1029/97JA00439